Journal of Power Sources 196 (2011) 5423–5431

Contents lists available at ScienceDirect

Journal of Power Sources

journal homepage: www.elsevier.com/locate/jpowsour

Electrochemical testing of suspension plasma sprayed solid oxide fuel cell electrolytes

D. Waldbillig [a], O. Kesler [b,*]

[a] University of British Columbia, Department of Materials Engineering, 309-6350 Stores Road, Vancouver, BC, Canada V6T 1Z4
[b] University of Toronto, Department of Mechanical and Industrial Engineering, 5 King's College Road, Toronto, Ontario, Canada M5S 3G8

ARTICLE INFO

Article history:
Received 11 January 2011
Received in revised form 11 February 2011
Accepted 17 February 2011
Available online 26 February 2011

Keywords:
Solid oxide fuel cell
Plasma spraying
Electrolyte
Electrochemical testing
Metal support
SOFC

ABSTRACT

Electrochemical performance of metal-supported plasma sprayed (PS) solid oxide fuel cells (SOFCs) was tested for three nominal electrolyte thicknesses and three electrolyte fabrication conditions to determine the effects of electrolyte thickness and microstructure on open circuit voltage (OCV) and series resistance (R_s). The measured OCV values were approximately 90% of the Nernst voltages, and electrolyte area specific resistances below 0.1 $\Omega\,cm^2$ were obtained at 750 °C for electrolyte thicknesses below 20 μm. Least-squares fitting was used to estimate the contributions to R_s of the YSZ bulk material, its microstructure, and the contact resistance between the current collectors and the cells. It was found that the 96% dense electrolyte layers produced from high plasma gas flow rate conditions had the lowest permeation rates, the highest OCV values, and the smallest electrolyte-related voltage losses. Optimal electrolyte thicknesses were determined for each electrolyte microstructure that would result in the lowest combination of OCV loss and voltage loss due to series resistance for operating voltages of 0.8 V and 0.7 V.

1. Introduction

Solid oxide fuel cells are a highly efficient technology that produces electricity and high temperature byproduct heat from a fuel source. SOFCs are able to use a wide variety of fuels and are inherently more tolerant to species such as carbon monoxide that poison other types of fuel cells due to the oxide ion conducting nature of the SOFC electrolyte, the high operating temperature, and the lack of a requirement for noble metal electrode catalysts. These qualities make SOFCs a promising near term energy production device.

Widespread adoption of SOFCs is mostly limited by durability and cost issues. One of the main sources of SOFC durability limitations is the inherent brittleness of the commonly used ceramic or cermet mechanical support layers. Stainless steel has been proposed as a potentially more robust support material [1]; however, it is difficult to fabricate metal supported SOFCs using the wet ceramic SOFC manufacturing processes, as the high temperature firing operations required to sinter and densify SOFC layers severely degrade the metal support. Sintering aids or inert atmosphere firing have been proposed as potential methods to reduce the support degradation during processing, but these methods may be detrimental to the electrolyte conductivity or expensive [2,3]. Infiltration methods have also been proposed as an alternative method to fabricate metal supported SOFCs [4]; however, these techniques are slow and may be quite difficult to scale up to the large manufacturing volumes required to bring down SOFC costs. At low production volumes, SOFC systems cost on the order of $10,000/kW [5], and while system costs are expected to decrease significantly as more efficient manufacturing processes are developed and scaled up, it will still be challenging to achieve the US Department of Energy's cost target of $400/kW [6] with wet ceramic cell fabrication processes.

Materials, equipment, and labour costs make up the majority of SOFC manufacturing costs. Material costs consist of the cost of the raw materials required to produce the SOFC support and electrochemically active layers. A recent economic study determined that material costs represent more than 50% of the total cell cost at sufficiently large production volumes for which the cost/kW converges to a stable value and that the cermet support layer for wet ceramic produced cells represents ~75% of the total material cost [5]. If metal supports are used, support layer costs can be decreased to ~12% of the total cost, which decreases the total cell cost by approximately 40%. In addition to being less expensive, metal supports also have superior mechanical, thermal and electrical properties compared to Ni/YSZ cermet supports. SOFC equipment costs at the low production volumes needed for early market entry may also be reduced by lowering the number and complexity of unit operations, and labour costs can be decreased by increasing the amount of automation in the manufacturing process.

* Corresponding author. Tel.: +1 416 978 3835; fax: +1 416 978 7753.
E-mail address: kesler@mie.utoronto.ca (O. Kesler).

0378-7753/$ – see front matter © 2011 Elsevier B.V. All rights reserved.
doi:10.1016/j.jpowsour.2011.02.057

Table 1
Electrolyte suspension plasma processing parameters.

Parameter	High flow rate	Medium flow rate	Low flow rate
Plasma gas flow rate (slpm)	275	250	230
Plasma gas composition (%)	70% N_2, 25% Ar, 5% H_2	80% N_2, 15% Ar 5% H_2	87% N_2, 13% Ar
Current (A per cathode)	250	250	250
Nozzle size (mm)	9.5	9.5	9.5
Preheat temperature (°C)	300–350	300–350	300–350
Standoff distance (mm)	90	80	80

Plasma spraying is a well-established manufacturing technique that can produce fully sintered ceramic coatings rapidly and without the need for post deposition heat treatments. This technique has been used for over 50 years to produce many different types of coatings such as the thermal barrier coatings in gas turbines. Plasma spraying can produce coatings extremely rapidly and is relatively easy to automate; however, this technique has difficulty producing coatings with high porosity (>25%) or low porosity (<10%) and in producing uniform coatings of less than 50 μm in thickness due to the large size of the feedstock particles (10 to several 100 μm). In order to enhance the ability of PS processes to control the microstructure and porosity and to enable thinner layers to be produced, a micron or sub-micron sized feedstock powder suspended in a carrier liquid can be used. This technique is called suspension plasma spraying (SPS) and has the potential to significantly improve coating quality and control while keeping the rapid deposition and lack of post deposition heat treatment requirement of conventional powder based PS processes. There are a number of groups throughout the world developing and characterizing SPS coatings for a variety of applications [7–11].

PS SOFCs have a number of potential cost and performance advantages compared to wet-ceramic SOFC manufacturing processes [12–15]. PS processes allow stainless steel mechanical supports to be used without any additional cost or performance trade-offs specific to the use of the metallic supports. The rapid deposition rate and elimination of high temperature firing operations allow for high throughputs, simple process flow, and easy automation, which lower process, equipment, and labour costs. PS processing can also realize significant cost savings even at fairly low production volumes due to the use of metal supports and to the scalability of the equipment requirements for different production levels [5]. In addition, the rapid nature of PS SOFC manufacturing may have the potential to improve SOFC performance by allowing higher performing or less expensive material sets that may interreact or decompose at the high temperatures required to sinter electrolyte layers to be used for electrochemically active layers, since the extremely rapid cooling of PS layers gives the layers little time for the normally diffusion-based inter-reactions to occur. Finally, PS processes may allow finer control over the composition, size or nature of functional layers, allowing these layers to be functionally graded in order to reduce thermal stresses, improve electrochemical properties, or enhance functional features such as internal reforming.

There are many groups throughout the world that are working to develop PS SOFC process [16–19]; however, much work is still required in order to determine the effects of PS parameters on SOFC layer microstructures and to characterize the effect of PS layer features such as splat boundaries on the electrochemical activity of PS SOFCs. This study investigates the electrochemical properties of SOFCs fabricated from three promising SPS conditions identified in a previous study [20] on porous ferritic stainless steel mechanical supports and examines the effect of electrolyte thickness and microstructure on the open circuit voltage (OCV) and series resistance (R_S) values. Three different nominal electrolyte thicknesses were tested (15 μm, 30 μm and 45 μm).

Cathode and anode layers were produced by conventional PS processes and are being optimized in parallel studies [21–23] and thus will only be briefly discussed in this work.

2. Experimental procedure

2.1. Substrate and feedstock material

SOFCs were deposited onto 2.54 cm diameter porous ferritic stainless steel 430 substrates with a media grade (MG) of 2 (Mott Corporation, Farmington, CT, USA). This substrate type is most commonly used as a filter medium, and the media grade designation refers to the smallest diameter particle in micrometers that can be captured in the filter.

A 48.2–51.8 wt% mixture of individually spray dried lanthanum strontium manganite ($La_{0.8}Sr_{0.2}MnO_{3-\delta}$, LSM) and 8 mol% yttria-stabilized zirconia (YSZ) powders (Inframat Advanced Materials, Farmington, CT, USA) was used for the cathode layers. Spray dried cathode powders were sieved and mechanically mixed before plasma spraying. The detailed cathode powder preparation procedure has been reported previously [21].

Non-spray dried 8 mol% YSZ powder (Inframat Advanced Materials, Farmington, CT, USA) was used as the electrolyte feedstock for this study. The as-received powder had a d_{50} agglomerate size of approximately 1.6 μm, with sizes ranging from 0.5 μm to 15 μm, as determined previously by laser light scattering (Mastersizer 2000, Malvern Instruments, Worcestershire, UK) [24]. Aqueous YSZ suspensions with a solid loading of 3 vol% (15.4 wt%) were prepared using deionized water and 0.01 wt% PBTCA (2-phosphonobutane-1,2,4-tricarboxylic acid) dispersant referenced to the ceramic solid weight.

A sprayed dried, pre-agglomerated mixture of 70 wt% NiO and 30 wt% YSZ powder (Inframat Advanced Materials, Farmington, CT, USA) was used for the anode layer feedstock. The anode powders were calcined at 1200 °C for 2 h to prevent agglomerate break up during feeding and then sieved. 9.3 wt% of a commercially available flour (Robin Hood All-purpose Flour, Smuckers Foods of Canada, Markham, ON, Canada) was added to the anode powder before plasma spraying to serve as a pore former.

2.2. Plasma spray processing

All SOFC layers were deposited using an axial injection APS system (Axial III Series 600, Northwest Mettech Corp., North Vancouver, BC, Canada) that was modified to deliver liquid suspensions using a pressured canister as described previously [24]. A needle type nozzle with an inner diameter of 0.84 mm that was positioned directly behind the torch convergence injected the suspension directly into the centre of the plasma jet, where it was atomized by the plasma plume. During SPS, the feedstock suspension was fed to the torch at a rate of 104 mL min^{-1}, which resulted in a total solid flow rate of 18.5 g min^{-1}.

During spraying runs, the substrates were mounted on a rotating turntable and the torch was moved vertically. Before the powder or suspension feeding systems were started, the substrates were preheated directly by the plasma torch to a temperature between

Table 2
Summary of sprayed electrolyte characteristics.

Spraying condition	Density (g cm^{-3}/%)	Permeation rate 30 ± 2 μm coating (cm^3 min^{-1})	Permeability (m^2)
High flow	5.7/96	0.30	9.21E−18
Medium flow	5.5/93	0.40	1.14E−17
Low flow	5.1/86	0.40	1.15E−17

300 and 350 °C, as measured directly by a Type K thermocouple in contact with the back surface of the metal substrate.

A plasma sprayed composite LSM/YSZ cathode layer was first deposited on the steel substrates at conditions described previously [21,24] and an SPS YSZ electrolyte layer was then deposited on top of the cathode layer. Suspension plasma sprayed electrolyte layers were produced from one of the three conditions listed in Table 1. The spraying conditions were labelled as having high, medium, or low flow rates, which indicates the relative plasma gas flow rates used. A previous study had determined that these conditions produced layers with promising microstructures and properties potentially beneficial for use in electrolytes [20]. Electrolytes having three nominal thicknesses of 15, 30, and 45 μm were produced, in order to examine the effect of electrolyte thickness on the physical and electrochemical properties of the cell. Finally, a 1.1 cm in diameter plasma sprayed NiO/YSZ anode layer was deposited on top of the electrolyte layer at conditions described previously [24].

2.3. Characterization of plasma sprayed layers

After YSZ layers were deposited, the coating density, permeation rate, and microstructure were characterized. These physical characterization results have been described in detail for these and additional plasma spray conditions in a previous study [20] and are summarized in Table 2, with the density column presenting both the value of density and the percentage of theoretical density. The theoretical density of 8 mol% YSZ is 5.96 g cm^{-3} [25]. Layer density was calculated by dividing the weight gain after electrolyte spraying runs by the coating area and the coating thickness as measured by scanning electron microscopy (SEM). Helium permeation measurements were performed using an in-house designed fixture. The supply of helium gas was regulated at a gauge pressure of 3.5 kPa and the flow through the sample was measured by a mass flow meter. This flow rate was then used to calculate the layer permeability using Darcy's law [24,26].

Polished cross sections of the deposited layers were examined in a Hitachi S-3000N SEM (Hitachi High Technologies America, Pleasanton, CA, USA). Samples were mounted in epoxy, cut using a low speed diamond saw, and then polished using diamond polishing suspensions. The polished samples were gold coated to provide sufficient conductivity for SEM imaging. The back-scattered electron (BSE) imaging mode was used for all SEM images in order to enhance the contrast between the individual SOFC component materials.

2.4. Electrochemical testing

2.4.1. Test equipment and contact

Single cell test stations (model FCSH-1000, Materials Mates Italia, Milan, Italy) with additional gas flow control hardware and software (Arbin Instruments, College Station, TX, USA) were used for electrochemical testing. Platinum mesh was used for both the anode and cathode side contacts.

2.4.2. Sealing

A two part sealing system was utilized for the electrochemical tests. First, a wet ceramic seal (Ceramabond 552-VFG, Aremco Products, Inc., Valley Cottage, NY) was painted on the outside edge of the cells in order to limit any leakage from the cell edges. The ceramabond seal was cured as per the included instructions [27]. A commercially available sealing product (Thermiculite 866, The Flexitallic Group, Houston, USA) was used to seal the face of the cell to the test station tube. An anode supported cell with a screen printed and fired electrolyte achieved an open circuit voltage of 1.02 V at 750 °C with a hydrogen concentration of 20% while using this sealing system.

2.4.3. Cell testing

Electrochemical tests were performed using a Solartron 1470E multi-channel potentiostat and 1260 frequency response analyzer (London Scientific, London, ON, Canada). Cells were first heated to 750 °C in a 4% H_2 atmosphere on the anode side and still air on the cathode side. Once the cell reached temperature, the H_2 concentration was slowly increased to 20% and flowing air was introduced on the cathode side. The reduction process continued until the cell open circuit voltage stopped rising, usually after approximately 1 h of reduction. The conditions used during cell testing are summarized in Table 3. Electrochemical tests were performed with high flow rates in order to overcome diffusion limitations caused by the design of the test station and by the lower than optimal electrode layer porosities. Anode gasses were humidified to 3% by passing the gasses through a humidifier containing de-ionized water at room temperature.

During electrochemical testing, polarization curves and impedance measurements were made at each testing temperature. Since this study is primarily focused on characterizing the electrochemical performance of the electrolyte layers, the focus of the electrochemical testing was to determine open circuit voltage (OCV) and series resistance values of the cells with different electrolytes. The open circuit voltage (OCV) determined from polarization curves provides information about electrolyte and seal permeability. Series resistance values obtained from the high frequency intercept of the Nyquist impedance plots provide information about the cell losses due to the electrolyte material and microstructural resistivity and any contact resistance present.

3. Results

3.1. Electrochemical testing

3.1.1. Polarization curves

Polarization curves were obtained from open circuit voltage to a voltage of 0.27 V at temperatures of 750, 700, 650 and 600 °C. Typical polarization curves of a cell sprayed at the high flow condition showing the voltage–current behaviour (solid lines, left axis) and power density (dashed lines, right axis) are shown in Fig. 1. In the figure it can be observed that the measured open circuit voltage is

Table 3
Electrochemical testing parameters.

Parameter	Value
Anode gas composition (vol%)	20% H_2, 80% N_2
Anode gas flow (sccm)	950
Cathode gas composition (vol%)	Air (79% N_2, 21% O_2)
Cathode gas flow (sccm)	950
Testing temperature (°C)	600, 650, 700, 750

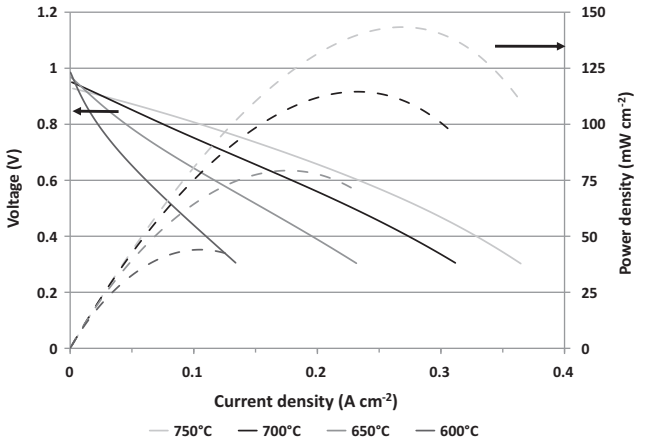

Fig. 1. Polarization curves for a typical tested cell fabricated at high gas flow conditions.

approximately 10% lower than the value predicted by thermodynamics and that further improvement of both the electrolyte and electrode layers is required. As expected, the cell open circuit voltage values increased as the temperature decreased and the slopes of the curves increased as the temperature decreased, indicating that the electrolyte and polarization resistances were increasing. The concave down nature of the polarization curves at higher current densities and temperatures suggested that there were significant mass transport losses present, which are likely attributable to a combination of low electrode porosity and poor test station gas feed design. A maximum power density of 0.14 W cm^{-2} at 750 °C was observed for the cells with SPS electrolytes produced with the high flow rate conditions. Maximum power density values found in the SOFC literature vary by more than 3 orders of magnitude from values of ~0.01 to >1 W cm^{-2} depending on the material sets used, microstructures, cell geometries, and testing conditions. The highest power density reported to date for an entirely thermally sprayed SOFC is ~0.4 mW cm^{-2} at 750 °C [28], although power densities of up to ~0.9 W cm^{-2} at 700 °C have been achieved for cells with plasma sprayed anode and electrolyte layers and screen printed cathode layers [29].

The effects of temperature and permeation rate on the cell open circuit voltage are shown in Fig. 2a for coatings produced from the high flow rate spraying condition. As expected, the cell open circuit voltage increases as the testing temperature decreases and as the electrolyte permeation rate decreases. Fig. 2b shows the effect of electrolyte permeation rate on the open circuit voltage at 750 °C for the three electrolyte microstructures examined. It can be seen in the figure that for equivalent permeation rates, the open circuit voltage values for the three microstructures were very similar, as expected. Microstructures produced in high flow rate plasma processing conditions were able to achieve lower permeation rates at equivalent thicknesses compared to the other two conditions at all thicknesses studied.

3.1.2. Impedance measurements

Impedance tests were performed at open circuit voltage for the four test temperatures. A blank impedance measurement with no cell loaded was performed for each test station in order to determine the amount of inductance present in the system due to the wires and test station in order to subtract this value from the measured impedance to isolate the cell impedance. Typical Nyquist impedance plots for a cell sprayed at the high flow condition are shown in Fig. 3. Fig. 3a shows the measurements before inductance correction, while Fig. 3b shows the same measurements after the inductance has been subtracted. Series resistance (R_s) values were

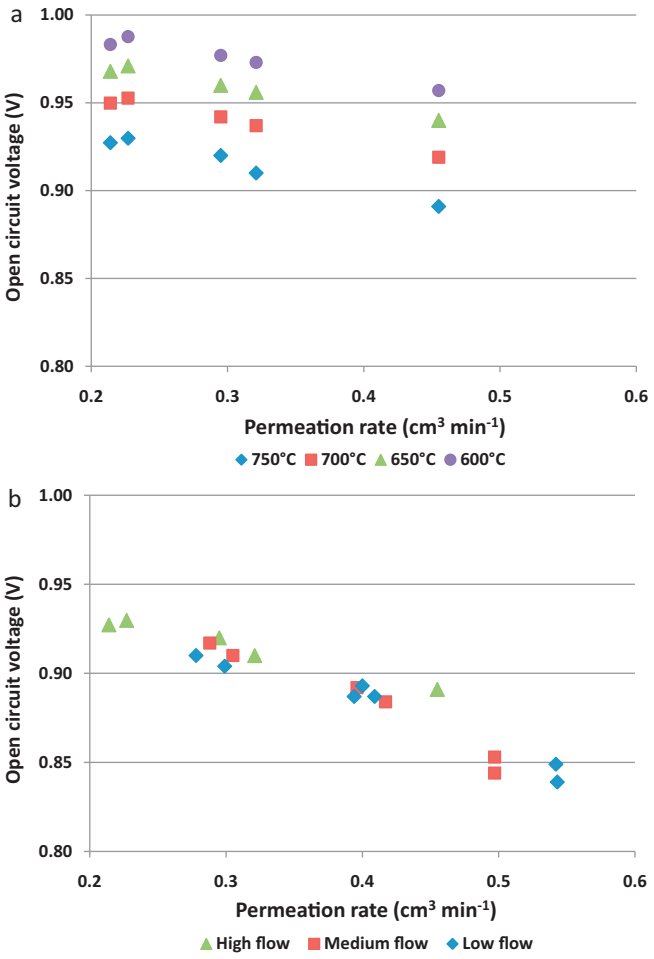

Fig. 2. Effect of permeation rate on the measured open circuit voltage of electrolyte layers with (a) high processing gas flow rate microstructures at temperatures of 600, 650, 700, and 750 °C with 20% H_2 and (b) low, medium and high processing gas flow rate microstructures at 750 °C with 20% H_2.

determined from the high frequency intercepts of the inductance corrected Nyquist plots. These values were separated into three main loss types: YSZ resistivity losses, microstructure based losses, and contact losses.

The effect of electrolyte thickness on the measured R_s values for cells produced at the high flow rate spraying condition is shown in Fig. 4 for the four test temperatures investigated. As expected, the R_s values increase as the thickness increases and as the temperatures decreases.

3.1.3. Series resistance separation

In order to better understand the root causes of the various electrolyte loss mechanisms, the series resistance (R_s) values measured during electrochemical testing were analyzed to estimate the relative contributions from each of 3 mechanisms to the overall series resistance, as shown in Eq. (1).

$$R_s = R_{YSZ} + R_\mu + R_C \quad (1)$$

In the equation, R_{YSZ} is defined as the area specific resistance caused by the limited ionic conductivity of YSZ and is calculated directly by dividing the electrolyte layer thickness by a literature value of YSZ conductivity [30]. R_μ is defined as the area specific resistance due to microstructural features within the electrolyte layer such as porosity or splat boundaries, while R_C is defined as the area specific resistance due to the contact interfaces present between the cell and test station. A least-squares fitting method

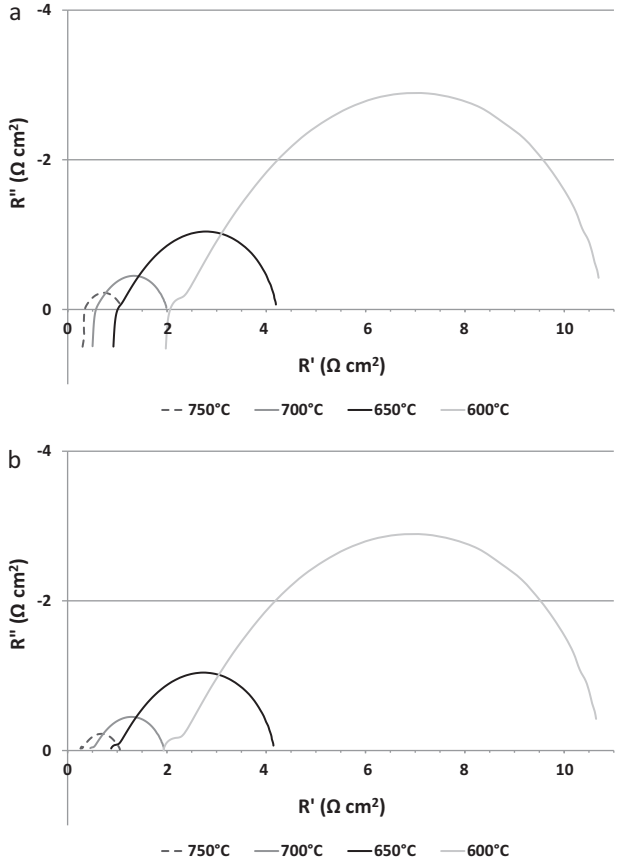

Fig. 3. Impedance curves (a) before and (b) after inductance subtraction for a cell produced from high flow rate spraying conditions.

was used to separate the relative contributions of R_μ and R_C. In order to enable the values from each test to be compared, a parameter called the microstructural resistivity value (ρ_μ) was defined, which represents the intrinsic resistivity of the electrolyte microstructural features (e.g. its splat boundaries), and thus is constant for a given test temperature and spraying condition (i.e. electrolyte microstructure). ρ_μ is calculated by dividing the R_μ value by the measured electrolyte thickness. For each comparable test (same temperature and spraying condition), ρ_μ values were set equal to each other and then the set of equations was solved

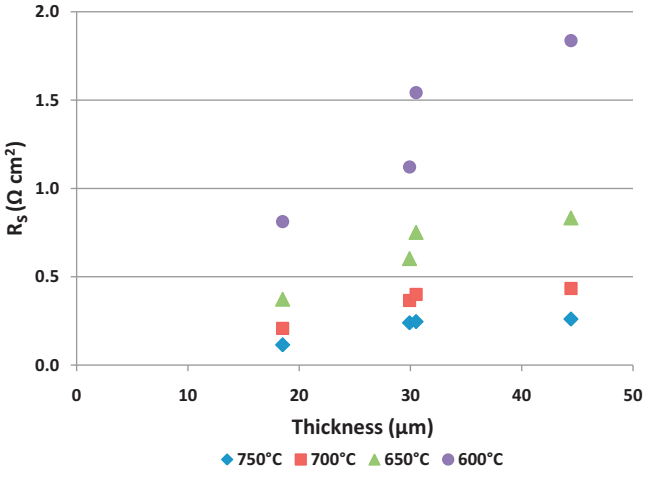

Fig. 4. Effect of thickness on the measured R_s value for high flow rate microstructures at temperatures of 600, 650, 700, and 750 °C with 20% H_2.

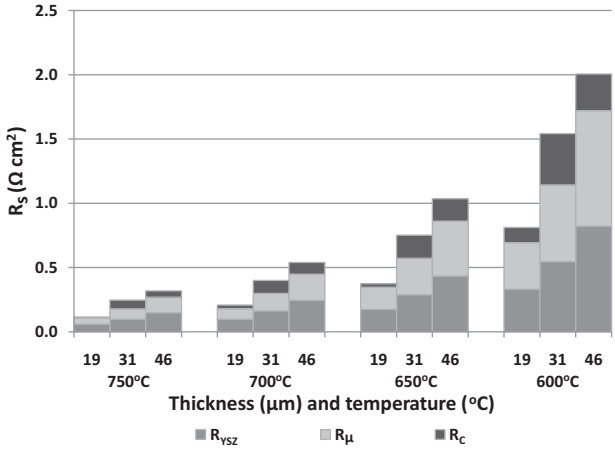

Fig. 5. Effect of thickness and temperature on the ASR_s breakdown for a cell sprayed at the high flow rate condition.

iteratively until the sum of the squared residual equations was minimized. This minimized residual point is where the most likely R_μ and R_C values for each tested cell occur. This procedure was then repeated for each electrolyte microstructure and testing temperature.

Fig. 5 shows an example of the resistance separation calculations for cells sprayed at the high flow rate condition. In the figure it can be observed that R_{YSZ} and R_μ increase as the temperature decreases or as the electrolyte thickness increases. The R_C value generally increases as the temperature decreases during each individual cell test; however, it is difficult to compare the contact resistance of different cell tests, as this resistance may be significantly affected by inherent test station differences, by variations in cell loading, and by cell-to-cell variations in parameters such as flatness or substrate oxide growth.

Characterizing the microstructural resistance of the electrolyte layer allows the effect of the microstructural features such as porosity and splat boundaries on the electrolyte performance to be quantified and enables the properties of different microstructures to be compared. A comparison of the microstructural resistivity (microstructural resistance divided by electrolyte layer thickness) of the three types of electrolyte layers at temperatures between 600 and 750 °C is shown in Fig. 6a. Electrolyte resistivity is strongly dependent on temperature and decreases by approximately an order of magnitude as the temperature increases from 600 to 750 °C. Electrolyte layers produced at the low flow rate condition had significantly higher resistivity than the other electrolyte types, possibly due to the greater amount of porosity present in the microstructure. Electrolytes sprayed at the medium flow condition had the lowest calculated microstructural resistivity, with values of less than 10 Ω cm at a temperature of 750 °C. A summary of the calculated total electrolyte area specific resistance ($R_{YSZ} + R_\mu$) for electrolyte thicknesses below 50 μm is shown in Fig. 6b. It can be seen in the figure that YSZ electrolytes produced from high or medium flow conditions have electrolyte layer area specific resistances of less than 0.1 Ω cm^2 at 750 °C for electrolyte thicknesses less than 20 μm.

3.1.4. YSZ conductivity comparison

The ionic conductivity value of plasma sprayed YSZ layers has been measured for coatings produced from various feedstock powders in this and other studies. In Fig. 7, the ionic conductivity of two plasma sprayed YSZ layers, the suspension plasma sprayed layers produced in this work, and a sintered YSZ electrolyte layer are compared as a function of temperature. Table 4 presents the conductivity values for the four YSZ layer types at 600 °C. The

Table 4
Ionic conductivity of PS, SPS and sintered YSZ layers at 600 °C.

Layer deposition method	Feedstock primary particle size	Conductivity (S cm^{-1})	Source
Plasma spray	5–25 μm	0.0006	[18]
Plasma spray	80–250 nm	0.0020	[19]
Suspension plasma spray	1 μm	0.0027	This work
Wet ceramic and sintered	Not reported	0.004	[20]

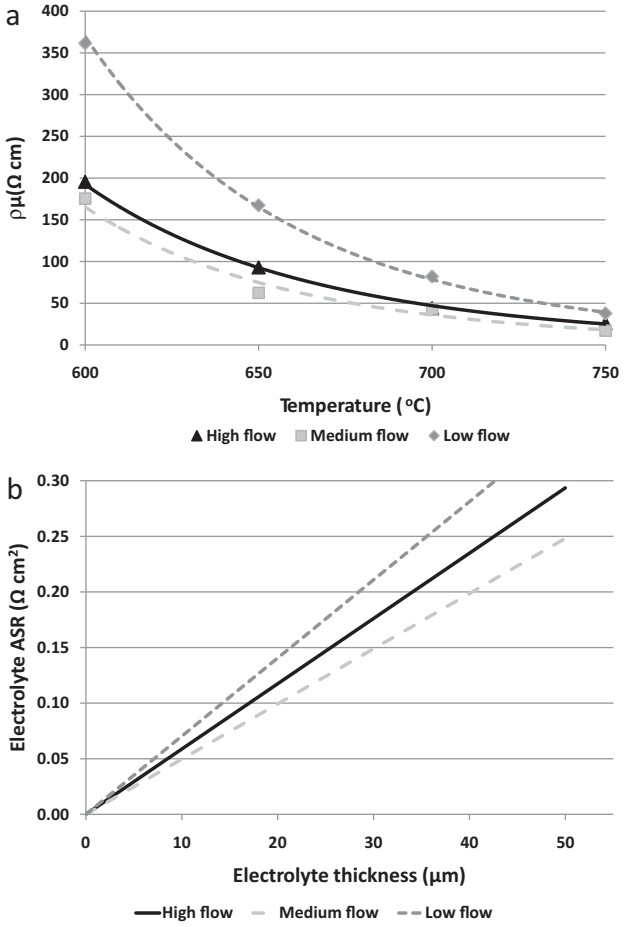

Fig. 6. Comparison of (a) the microstructural resistivity of electrolyte layers sprayed at three conditions for temperatures between 600 and 750 °C and (b) the total area specific resistance of electrolyte layers sprayed at three conditions for various thicknesses at 750 °C.

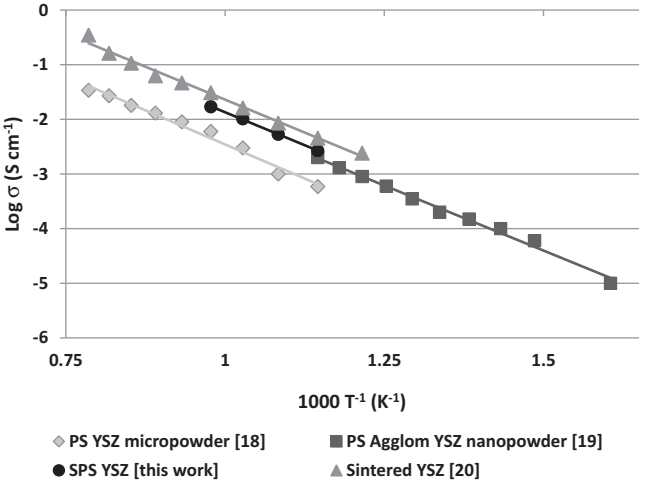

Fig. 7. Comparison of the total ionic conductivity of PS and sintered YSZ layers.

plasma sprayed YSZ layers were produced either from 8 mol% YSZ feedstock powders between 5 and 25 μm in size [31] or from nanocrystalline 10 mol% YSZ powders consisting of primary particles 80–250 nm in size that had been spray dried into spherical agglomerates 10–50 μm in diameter [32]. It can be seen in the figure and table that the SPS YSZ layer has a higher conductivity value compared to the other PS YSZ layers, but that the conductivity is lower than that of the sintered YSZ layer. This lower conductivity value may be due to the presence of defects such as pores and other microstructural defects within the SPS YSZ layer.

Fig. 8 shows a comparison between literature grain and grain boundary conductivity values for a sintered YSZ layer [33] and the microstructural conductivity values calculated for the three suspension plasma sprayed (SPS) microstructures (high flow rate, medium flow rate, and low flow rate) studied in this work. As can be seen in the figure, the SPS microstructural conductivities that were calculated were between 2.5 and 5 times higher than the literature grain boundary conductivity values.

The graphs shown in Fig. 8 illustrate the total value of grain, grain boundary, and microstructural conductivities; however, the spatial frequencies of the grain boundaries and microstructural features such as splat boundaries in the two coating microstructures differ and thus need to be compensated in order to compare the intrinsic grain boundary and microstructural contributions to the coating resistivities. For a certain layer thickness (e.g. 10 μm), the total area specific resistance (ASR, Ω cm^2) for the grain boundaries and microstructural features can be estimated by approximating the microstructures as a series of "bricks" or grains with parallel sides, connected by "mortar", i.e. grain boundaries or splat boundaries.

If we assume that the influence of porosity is minimal, as the SPS electrolyte layers produced in high plasma flow rate conditions contain less than 5% porosity [25], and that there are few Si-containing blocking phases at the SPS grain boundaries due to the purity of the powder and small amount of time the SPS coating is at elevated temperatures, which limits the ability of Si to diffuse to the grain boundaries, the most influential remaining component

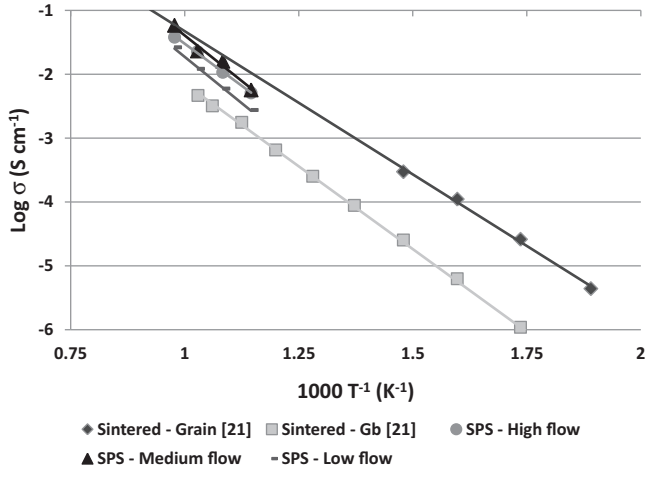

Fig. 8. Comparison of the grain, grain boundary (Gb), and microstructural conductivities for sintered and SPS YSZ layers.

Table 5
Intrinsic grain boundary and splat boundary ASR per defect calculation for 10 μm thick sintered and SPS YSZ layers at 700 °C.

	Sintered YSZ	High flow rate SPS YSZ
Total grain boundary or microstructural conductivity (S cm^{-1})	0.0046	0.023
Total grain boundary or microstructural ASR for a 10 μm thick coating (Ω cm^2)	0.22	0.044
Grain size (sintered) or splat size (SPS) (μm)	0.045 [21]	1 (from SEM)
Approximate defect frequency in a 10 μm thick layer	220	10
Grain boundary or splat boundary intrinsic ASR (Ω cm^2 per defect)	0.00098	0.004

of the microstructural resistivity is likely to be the splat boundaries.

For a certain coating thickness, the frequency of defects (grain boundaries in the sintered layer and splat boundaries in the SPS layer in the direction perpendicular to the coating) can be calculated by dividing the coating thickness by the grain size and adding 1. The grain size of the sintered layer was estimated to be ~45 nm [34] and the splat size of the high flow rate SPS layer was estimated to be ~1 μm (from SEM images). If the total area specific resistance contribution from each defect type (grain boundary or splat boundary) is then divided by this defect frequency, the intrinsic grain boundary and splat boundary ASR per defect can be estimated.

Calculation results of the intrinsic grain boundary and splat boundary ASR per defect are shown in Table 5. It can be seen in the table that although the total grain boundary conductivity is approximately 5 times smaller than the total microstructural conductivity value (or total ASR value is 5 times larger), when this value is normalized to account for the number of defects present within each coating, the calculated intrinsic grain boundary ASR is actually approximately 4 times smaller than the intrinsic splat boundary ASR.

3.1.5. Operating point calculations

For electrolyte layers that contain a measurable amount of permeability, the electrolyte thickness resulting in the lowest voltage losses should be chosen for a given electrolyte microstructure and its corresponding permeability to maximize cell performance. Therefore, in order to better understand the cumulative effect of gas leakage and electrolyte resistance losses on the cell operating voltage, the total amount of voltage loss (ΔV) was calculated by the summation of the open circuit voltage losses and voltage losses resulting from the series resistance contributions of both the bulk electrolyte material and electrolyte microstructure (Eq. (2)) for two common operating points, 0.7 V and 0.8 V.

$$\Delta V_x = V_{\text{Leak}} + V_{\text{YSZ},x} + V_{\mu,x} \quad (2)$$

In Eq. (2), x is the operating voltage. V_{Leak} is defined as the difference between the calculated Nernst voltage (E_{Ideal}) at the test temperature and hydrogen concentration of interest and the measured open circuit voltage (V_{OCV}). This voltage loss is caused by leakages within the cell, seals, and test equipment. V_{YSZ} is defined as the bulk YSZ material resistance (R_{YSZ}) multiplied by the current density measured from a polarization curve at the operating point of interest ($i_{0.8\,\text{V}}$ or $i_{0.7\,\text{V}}$). This voltage loss decreases as the electrolyte thickness is decreased. V_μ is defined as the electrolyte resistance due to the microstructural features within the electrolyte layer such as porosity or splat boundaries (R_μ) multiplied by the current density measured from a polarization curve at the operating point of interest ($i_{0.8\,\text{V}}$ or $i_{0.7\,\text{V}}$). This voltage loss decreases as the electrolyte thickness is decreased and varies for electrolytes sprayed at different conditions, which have different microstructures.

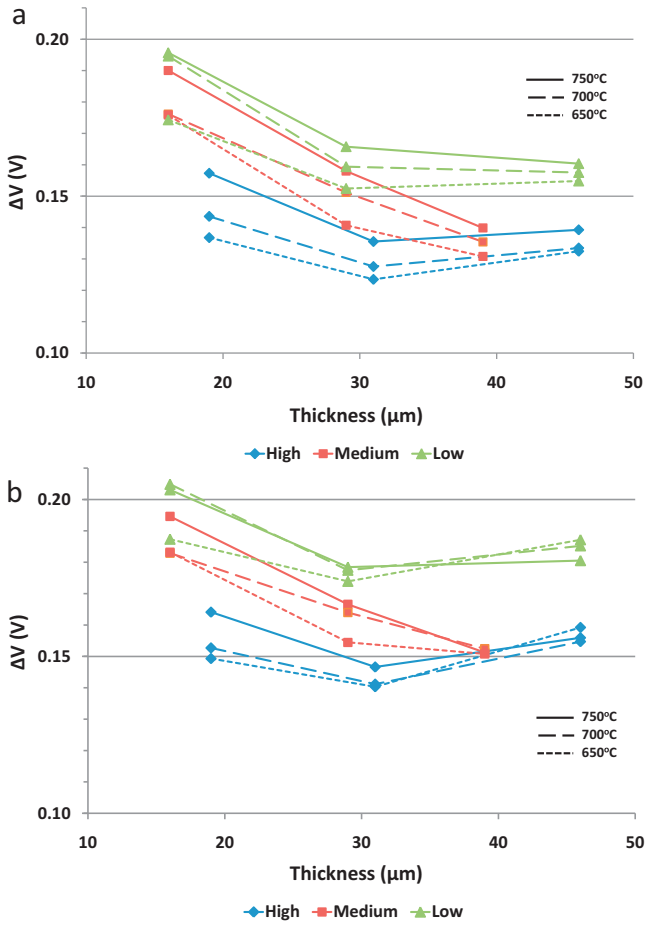

Fig. 9. Calculated ΔV values for cells sprayed at high, medium, and low flow rate conditions at various electrolyte thicknesses and testing temperatures and an operating point of (a) 0.8 V and (b) 0.7 V.

The calculated ΔV values for cells sprayed at the high, medium, and low flow rate conditions are shown in Fig. 9 as a function of cell thickness for cell testing temperatures of 650, 700, 750 °C. In Fig. 9a, an operating point of 0.8 V is shown, while in Fig. 9b an operating point of 0.7 V is shown. For the highly dense microstructures produced from the high flow conditions, intermediate thicknesses (~30 μm) produced the lowest ΔV for both operating voltages and all temperatures investigated due to the low permeabilities of the layers produced from these conditions. For coatings produced from the medium flow rate spraying conditions, the thickest electrolyte layers had the lowest ΔV for both operating voltages and at all temperatures investigated. Thicker electrolyte layers may be favoured for these microstructures due to the low microstructural resistivity and higher permeabilities of these electrolyte microstructures. The ΔV trends seen for the low flow rate microstructures illustrate the competing loss mechanisms of leakage and microstructural resistivity. At an operating voltage of 0.8 V and temperatures of 700 or 750 °C, the effect of leakage is more significant than the microstructural resistivity; therefore, the thickest electrolyte layers produce the lowest ΔV values. However, at lower temperatures (650 °C), the effect of microstructural resistance became more significant since the electrolyte conductivity is lower at the low temperature, and the lowest ΔV values were observed at the intermediate electrolyte thicknesses. At an operating voltage of 0.7 V, the lowest ΔV values were observed at the intermediate electrolyte thicknesses. This indicates that the voltage drop due to the increase in

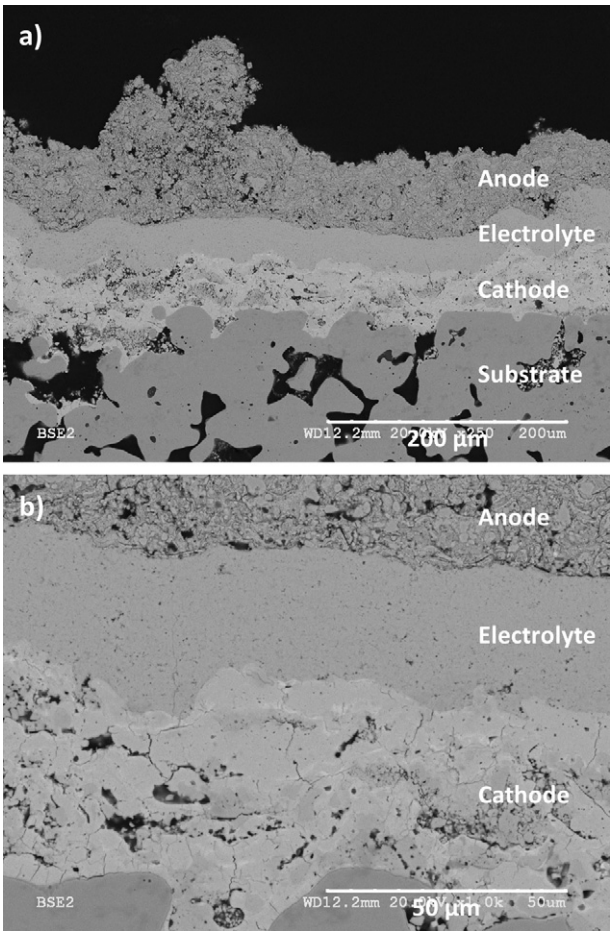

Fig. 10. BSE SEM images of typical high flow condition microstructures at: (a) 250× magnification and (b) 1000× magnification..

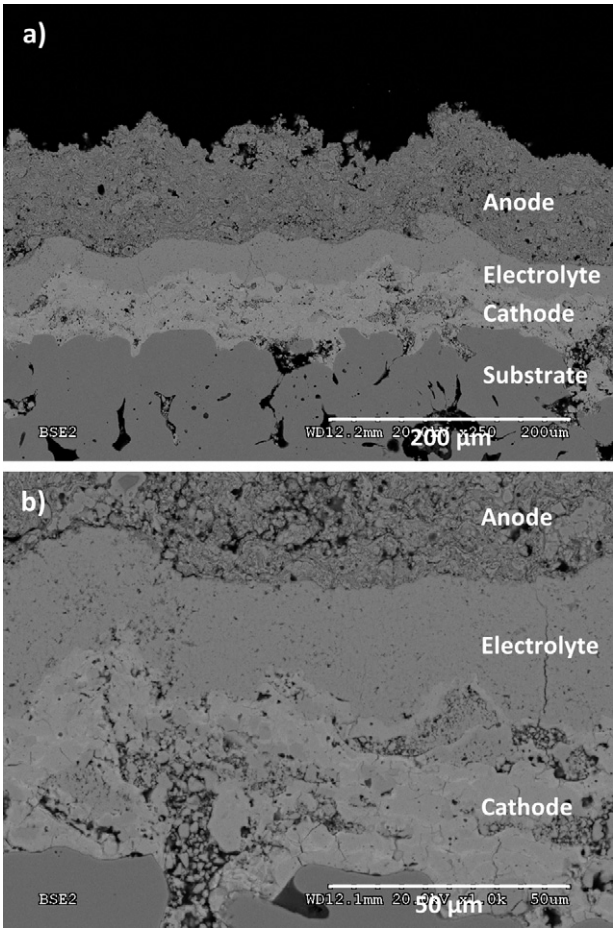

Fig. 11. BSE SEM images of typical medium flow rate condition microstructures at: (a) 250× magnification and (b) 1000× magnification..

the microstructural resistivity was more significant than that due to gas leakage across the electrolyte, seals, and test station for these conditions.

Broadly speaking, these calculations illustrate the importance of considering the cell operating conditions before choosing the best electrolyte layer thickness to use for electrolytes with non-zero permeabilities. At the higher operating temperatures (i.e. 700, 750 °C) minimal ΔV values were seen for thicker electrolytes that minimize electrolyte permeability losses. However, at the lower operating temperature (i.e. 650 °C), permeability losses are less significant and minimal ΔV values are seen for thinner electrolytes that have lower electrolyte resistive losses. For 0.8 V operating conditions, leakage losses are more significant, causing thicker, less permeable coatings to have lower ΔV values. At operating voltages of 0.7 V, electrolyte resistance losses become more significant, favouring thinner, less resistive electrolyte layers.

3.2. Microstructural analysis

SEM images of typical cross-sectional microstructures for the SOFCs produced at the high, medium, and low flow rate electrolyte spraying conditions after fuel cell testing are shown in Figs. 10–12, respectively. Cathodes and anodes were sprayed under identical conditions, and it can be seen in Figs. 10–12 that there is little cell-to-cell variation in cathode and anode layer thickness or microstructure. The cathode layer components (LSM and YSZ) were well mixed, there was some porosity present in the layers, and the cathode layers were able to fill and cover the large, deep pores present in the support material. There was excellent coverage and strong adhesion between the stainless steel support, cathode and electrolyte layers, even after a number of slow thermal cycles introduced during cell testing. Anode layers were quite thick and had unevenly distributed porosity. The larger, unevenly distributed pores present in the anode layer are likely due to the flour pore former used, while the smaller, more evenly distributed pores present are likely due to the porosity introduced when the sprayed NiO is reduced. Small detached areas (see Fig. 12b) were occasionally present at the electrolyte–anode interface. These areas may have been caused by the decrease in the anode layer volume as it was reduced or by thermal cycling effects during cell testing. Both anode and cathode layers likely have insufficient porosity for high cell performance, as seen by the diffusion limitations present in the electrochemical testing at the higher temperatures and current densities. Further electrode material and microstructural development is being performed in separate studies.

Electrolyte layers were reasonably dense, with three main defect types: vertical cracking, medium-sized defects, and small pores. Vertical cracking was likely caused by thermally induced residual stresses produced during spraying, the medium sized defects may be caused by unmelted particles present within the deposited layer or by cathode layer surface topography (see Fig. 11b), and the small pores present are likely intersplat porosity, visible in all coatings. Qualitatively, electrolyte layers produced from high flow conditions appeared to be the most dense, followed by those produced by medium and low flow conditions. This density trend was confirmed both by permeation rate and density measurements done previously [20] and by open circuit voltage measurements done in this work.

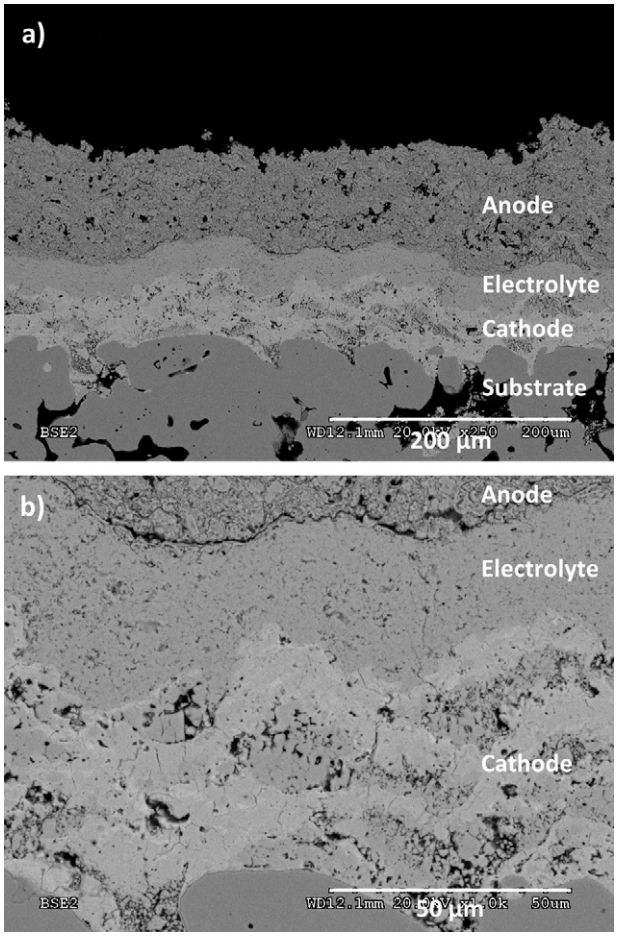

Fig. 12. BSE SEM images of typical low flow rate condition microstructures at: (a) 250× magnification and (b) 1000× magnification.

4. Conclusion

Metal supported plasma sprayed (PS) SOFC fabrication techniques have the potential to overcome many of the cost and durability issues that have held back widespread adoption of SOFCs. This study characterized the electrochemical performance of PS SOFCs with three different electrolyte microstructures and thicknesses in order to determine the effects of electrolyte thickness and microstructure on electrochemical properties such as open circuit voltage (OCV) and series resistance (R_s). Metal supported PS SOFCs were produced with OCV values approximately 10% lower than the OCV values predicted by thermodynamics and with electrolyte area specific resistances of <0.1 $\Omega\,cm^2$ at 750 °C for electrolyte thicknesses <20 μm. In order to better understand the root causes of the various electrolyte losses, measured R_s values were separated into YSZ material resistance losses, electrolyte microstructural resistance losses, and contact resistance losses. The highly dense electrolyte layers produced from high plasma gas flow rate conditions had the lowest permeation rates, the highest OCV values, and the lowest total electrolyte-related losses. Medium flow rate conditions produced more permeable electrolyte layers that had lower OCV values and higher total electrolyte-related losses than the high flow rate microstructures; however, these electrolyte layers had the lowest microstructural resistivities. Low flow rate coatings had poor electrolyte microstructures with high permeabilities, low OCV values, high total R_s, and high microstructural resistivities. In order to better understand the combined effect of gas leakage and electrolyte resistance losses on the cell voltage, the OCV and R_s losses were calculated for operating points of 0.8 V and 0.7 V and temperatures between 650 and 750 °C. These calculations may allow an electrolyte thickness that minimizes the voltage losses to be chosen for each operating point and electrolyte microstructure.

Acknowledgements

The authors gratefully acknowledge financial support from the Natural Sciences and Engineering Research Council of Canada, Northwest Mettech Corporation, and the BC Innovation Council, the Flexitallic Group for providing seal samples, and the helpful assistance of Craig Metcalfe, Joel Kuhn, and Michael Poon.

References

[1] Z.G. Yang, International Materials Reviews 53 (1) (2008) 39–54.
[2] M.J. Verkerk, A.J.A. Winnubst, A.J. Burggraaf, Journal of Materials Science 17 (11) (1982) 3113–3122.
[3] X. Zhang, C. Deces-Petit, S. Yick, M. Robertson, O. Kesler, R. Maric, D. Ghosh, Journal of Power Sources 162 (1) (2006) 480–485.
[4] J.M. Vohs, R.J. Gorte, Advanced Materials 21 (9) (2009) 943–956.
[5] D. Gallagher, Process Cost Modeling of Solid Oxide Fuel Cell Manufacturing, Master of Engineering Project Report, University of Toronto, Toronto, ON, Canada, 2009.
[6] Department of Energy—Fossil Energy: DOE's Fuel Cell R&D Program. http://www.fossil.energy.gov/programs/powersystems/fuelcells (accessed 01.05.10).
[7] R. Vassen, H. Kassner, G. Mauer, D. Stover, Journal of Thermal Spray Technology 19 (1–2) (2010) 219–225.
[8] P. Fauchais, R. Etchart-Salas, C. Delbos, M. Tognonvi, V. Rat, J.F. Coudert, T. Chartier, Journal of Physics D: Applied Physics 40 (8) (2007) 2394–2406.
[9] R. Rampon, C. Filiatre, G. Bertrand, Journal of Thermal Spray Technology 17 (1) (2008) 105–114.
[10] L. Jia, F. Gitzhofer, Journal of Thermal Spray Technology 19 (3) (2010) 566–574.
[11] J. Oberste Berghaus, J.G. Legoux, C. Moreau, R. Hui, C. Deces-Petit, W. Qu, S. Yick, Z. Wang, R. Maric, D. Ghosh, Journal of Thermal Spray Technology 17 (5–6) (2008) 700–707.
[12] R. Hui, Z. Wang, O. Kesler, L. Rose, J. Jankovic, S. Yick, R. Maric, D. Ghosh, Journal of Power Sources 170 (2) (2007) 308–323.
[13] R. Henne, Journal of Thermal Spray Technology 16 (3) (2007) 381–403.
[14] N.H. Menzler, F. Tietz, S. Uhlenbruck, H.P. Buchkremer, D. Stover, Journal of Material Science 45 (12) (2010) 3109–3135.
[15] M.C. Tucker, Journal of Power Sources 195 (15) (2010) 4570–4582.
[16] A.A. Syed, Z. Ilhan, J. Arnold, G. Schiller, H. Weckmann, Journal of Thermal Spray Technology 15 (4) (2006) 617–622.
[17] R. Vassen, D. Hathiramani, J. Mertens, V.A.C. Haanappel, I.C. Vinke, Surface & Coatings Technology 202 (3) (2007) 499–508.
[18] R. Hui, J.O. Berghaus, C. Decès-Petit, W. Qu, S. Yick, J.G. Legoux, C. Moreau, Journal of Power Sources 191 (2) (2009) 371–376.
[19] C. Zhang, H.L. Liao, W.Y. Li, G. Zhang, C. Coddet, C.J. Li, C.X. Li, X.J. Ning, Journal of Thermal Spray Technology 15 (4) (2006) 598–603.
[20] D. Waldbillig, O. Kesler, Effect of suspension plasma spraying process parameters on YSZ coating microstructure and permeability, forthcoming.
[21] B.D. White, O. Kesler, L. Rose, Journal of Power Sources 178 (1) (2008) 334–343.
[22] J. Harris, O. Kesler, Journal of Thermal Spray Technology 19 (1–2) (2010) 328–335.
[23] N. Benoved, O. Kesler, Journal of Power Sources 193 (2) (2009) 454–461.
[24] D. Waldbillig, O. Kesler, Journal of Power Sources 191 (2) (2009) 320–329.
[25] I.R. Gibson, G.P. Dransfield, J.T.S. Irvine, Journal of Materials Science 33 (17) (1998) 4297–4305.
[26] A.C. Fox, T.W. Clyne, Surface & Coatings Technology 184 (2–3) (2004) 311–321.
[27] Aremco: high temperature adhesives, ceramics, potting compounds, sealants, screen printers, dicing saws, furnaces. http://www.aremco.com/a2.html (accessed 01.05.10).
[28] M. Lang, T. Franco, G. Schiller, N. Wagner, Journal of Applied Electrochemistry 32 (2002) 871–874.
[29] R. Hui, J. Oberste Berghaus, C. Decès-Petit, W. Qu, S. Yick, J.G. Legoux, C. Moreau, Journal of Power Sources 191 (2) (2009) 371–376.
[30] A. Weber, E. Ivers-Tiffee, Journal of Power Sources 127 (1–2) (2004) 273–283.
[31] C. Zhang, C.J. Li, G. Zhang, X.J. Ning, C.X. Li, H. Liao, C. Coddet, Materials Science and Engineering B 137 (1–3) (2007) 24–30.
[32] Y. Chen, S. Omar, A.K. Keshri, K. Balani, K. Babu, J.C. Nino, S. Seal, A. Agarwal, Scripta Materialia 60 (11) (2009) 1023–1026.
[33] J.W. Fergus, Journal of Power Sources 162 (1) (2006) 30–40.
[34] H.J. Park, Y.H. Choa, Electrochemical and Solid-State Letters 13 (5) (2010) K49–K52.